General formulation of the magnetostatic field and temperature distribution in electrical machines using spectral element analysis

General Formulation of the Magnetostatic Field and Temperature Distribution in Electrical Machines Using Spectral Element Analysis

M. Curti, T.A. van Beek, J.W. Jansen, B.L.J. Gysen and E.A. Lomonova
Electrical Engineering, Electromechanics and Power Electronics
Eindhoven University of Technology
Eindhoven, The Netherlands
m.curti@tue.nl

In this paper, a general approach to the description of the magnetic field and temperature distribution in electrical machines using the spectral element analysis is presented. In the spectral element method, higher order Legendre-Gauss-Lobatto polynomials are applied to describe the different fields. The magnetic flux distribution is derived using the magnetic vector potential and nonlinear magnetic material is modeled based on its BH-curve. The thermal model is based on the heat equation. The magnetic and thermal domains are coupled by the ohmic and iron losses, the latter is computed using the loss separation model of Bertotti. The results are compared with FEM and a good agreement is obtained for both the spatial magnetic flux density and the temperature distributions.

***Index Terms*—Finite Element Method, Spectral Element Method, Iron losses, Thermal Model.**

I. Introduction

COMPREHENSIVE modeling of the electromagnetic field and temperature distributions in electrical machines is imperative in designing and developing electrical machines and actuators. Over the years, research and development focused on the prediction of the magnetic field and temperature distributions in electromagnetic devices. Several numerical and semi-analytical techniques exist in the literature such as the Finite Element Method (FEM), lumped parameter modeling, boundary element method, Schwarz-Christroffel mapping or harmonic modeling [1]–[6].

The preferred modeling technique is a trade-off between the desired accuracy and the computational effort which inherently depends on the type of problem [7], [8]. A subset of the mentioned methods requires discretization and meshing of the geometry prior to the calculation of the magnetic field and temperature distribution [9]. Accurate field descriptions can be obtained by increasing the mesh density, but this negatively affects the computation time. Furthermore, obtaining a solution for electromagnetic devices which have a large size and a small airgap becomes challenging due to the necessity of a high mesh density.

Alternatively, spectral methods employ comparatively fewer elements with higher-order expansions whereas finite element techniques apply many elements and expand each element into a low order. Furthermore, in the Spectral Element Method (SEM) the computational error decreases exponentially whereas in the finite element method the error decreases linear with the degrees of freedom [10]. Due to the fast convergence rate, the spectral element method requires fewer degrees of freedom to obtain the solution with a desired accuracy compared to methods that apply lower-order expansions. The spectral element method is well known in other engineering fields with high complexity such as wave scattering, structural analysis and fluid dynamics [11], [12] which include problems with high aspect ratios [13] or require a multi-physical approach [14]. Therefore, the spectral element method is suitable for modeling coupled problems, that have complicated arrangements of materials, without mesh adaptations between physical domains.

In this paper, the general formulation of the spectral element method is given and applied for a coupled magnetic-thermal problem. The presented spectral element formulation is applied for 2-D problems in the Cartesian coordinate system. Legendre-Gauss-Lobatto polynomials are employed to provide higher-order expansions of the solution in an element. Nonsquared or elements with curved boundaries are taken into account by applying the transfinite interpolation method. The spectral element method is compared with 2-D finite element analysis (Altair FLUX2D [15]) on a periodic section of a synchronous linear motor for both the electromagnetic and thermal domains. Nonlinear behavior of the soft-magnetic parts is taken into account iteratively. Distinction is made between the different types of boundary conditions and their implementation in the different domains. Furthermore, convergence analysis and the computational load of the spectral element method will be addressed.

II. Modeling approach

In the presented formulation of the spectral element method, the nodal Galerkin approximation is applied. This results in the weak formulation of the elliptic partial differential equation for a single computational element, which is a square with limits $[-1, 1]^2$. In order to incorporate nonsquared and curved elements, a transformation is applied from the computational element to the desired physical element. Consecutively, contravariant base vectors are introduced to incorporate the vector operations under transformation.

A. General formulation

Both the magnetic vector potential and the temperature distribution can be obtained in steady-state by solving the following form of the elliptic equation,

$$\nabla \cdot (c\nabla\varphi) = s, \tag{1}$$

where c and s are material coefficients and source descriptions. If c and s are functions of φ then (1) becomes nonlinear. For magnetic and thermal domains, (1) is rewritten in different forms. In the case of a 2-D, Cartesian, magnetostatic domain, φ represents the z-component of the vector magnetic potential $\vec{A}$, c represents the reluctivity, ν, defined as $1/\mu$, where μ is the permeability of the material. The magnetic field sources, such as coils with a current density, J_z, and permanent magnets with a magnetization, $\vec{M}_0$, are substituted in s,

$$\nabla \cdot (\nu\nabla A_z) = J_z + \nabla \times (\nu\mu_0\vec{M}_0). \tag{2}$$

In the case of the thermal domain, the potential, φ, represents the temperature distribution, T. The coefficient, c, represents the thermal conductivity of the material, k, and the coefficient, s, represents the source of the heat, $-g$, [16]. In this case, (1) becomes the heat equation

$$\nabla \cdot (k\nabla T) = -g. \tag{3}$$

B. Nodal Galerkin formulation

Applying the nodal Galerkin formulation to (1) results in the separation of boundary and surface integrals which allows boundary conditions to be taken into account by manipulation of the boundary integral. To obtain the weak form, the strong form, as presented in (1), is multiplied by a smooth function, β, which satisfies the boundary conditions and is integrated over the domain. Furthermore, by applying Green's first identity the following expression is obtained

$$\oint_{\partial\Omega_{\xi,\eta}} c\nabla\varphi \cdot \hat{n}\beta \mathrm{d}l - \iint_{\Omega_{\xi,\eta}} \nabla\beta \cdot (c\nabla\varphi)\mathrm{d}\Omega_{\xi,\eta} = \iint_{\Omega_{\xi,\eta}} s\beta \mathrm{d}\Omega_{\xi,\eta}, \tag{4}$$

where $\Omega_{\xi,\eta}$ represent the surface of the computational element with coordinate axes ξ and η.

For nonsquared or curved elements, a mapping transforms the computational element, $\Omega_{\xi,\eta}$, into the physical domain, $\Omega_{x,y}$. Under mapping, the vector operations are transformed based on the chain rule. The contravariant base vectors F^1 and F^2 and normal flux vector F_n are introduced to obtain the mapped vector operations without requiring the inverse of the transformation [17], [18]. As a result, the weak form of (1) for curved domains is given by

$$\begin{aligned} &\oint_{\partial\Omega_{x,y}} F_n\beta \mathrm{d}l - \iint_{\Omega_{x,y}} \left(F^1 \frac{\partial\beta}{\partial\xi} + F^2 \frac{\partial\beta}{\partial\eta} \right) \mathrm{d}\Omega_{x,y} \\ &\quad = \iint_{\Omega_{x,y}} sJ_T\beta \mathrm{d}\Omega_{x,y}, \end{aligned} \tag{5}$$

where J_T is the determinant of the Jacobian for the transformation. The derivation of the nodal Galerkin formulation for non squared geometries is given in detail in the Appendix A. To apply the Galerkin formulation on (5), the solution is approximated with a set of polynomial basis functions in each element. The derivative operators are replaced by derivative matrices and integrals by Gaussian quadratures which are discussed in the Section III.

III. Spectral Element Method

A. Legendre basis functions

In complex geometries, many elements with different material properties are present. Consequently, multiple elements are coupled by means of boundary conditions. In case of the SEM implementation applied in this paper, each element is discretized in a set of points which coincide with the roots of Legendre-Gauss-Lobatto (LGL) polynomial with degree N, P_{LGL}, given by

$$P_{LGL} = L_{N+1} - L_{N-1}, \tag{6}$$

where L_N is the N^{th}-degree Legendre polynomial which can be represented as three-term recursion

$$L_{N+1}(\xi) = \frac{2N+1}{N+1}\xi L_N(\xi) - \frac{N}{N+1}L_{N-1}(\xi), \tag{7}$$

with $L_0 = 1$ and $L_1 = \xi$. The roots of the LGL nodes from (6) are stored in a column vector,

$$\boldsymbol{\xi} = \begin{bmatrix} \xi_0, & \xi_1, & \ldots & \xi_N \end{bmatrix}^T. \tag{8}$$

Hence, for a Legendre polynomial with degree N, $N+1$ roots are obtained. In Fig. 1a, the root distribution of a 1-D element

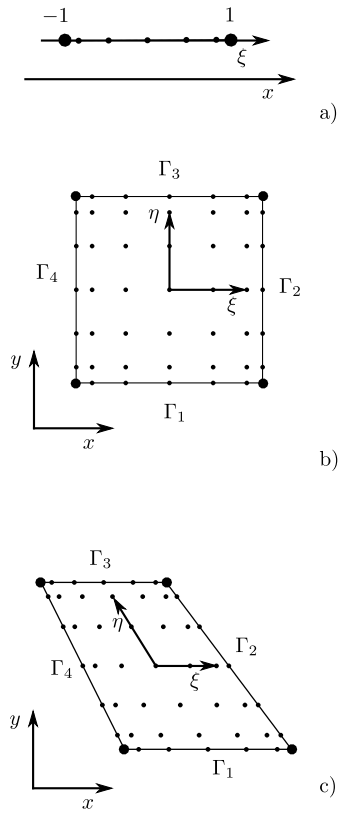

Fig. 1. The discretization of the elements into $N = 6$ LGL nodes a) A 1-D element with the local coordinate system ξ. b) A 2-D, square, element with coordinate system ξ, η. c) A 2-D nonsquared element.

is shown for N equal to 6, indicated by the black dots along the ξ-axis. Independent of the degree of the LGL polynomial, roots exist at the vertices of the domain, ξ equal to -1 and 1 respectively. Similarly, for a 2-D element, as shown in Fig. 1b, roots exist at the boundaries of the domain. This simplifies the implementation of boundary conditions between adjacent elements since the roots of shared boundaries coincide. The Lagrangian interpolation of a function f, that is approximated by a Legendre-Gauss-Lobatto polynomial, ensures the uniqueness of function f. The Lagragian interpolation of f is given by

$$f(\xi) = \sum_{j=0}^{N} f_j l_j(\xi), \tag{9}$$

where

$$l_j(\xi) = \prod_{\substack{n=0 \\ n\neq j}}^{N} \frac{\xi - \xi_n}{\xi_j - \xi_n}, \tag{10}$$

where f_j is the result of f, evaluated at the corresponding root. On each LGL root, for a 1-D element, the derivative of a function f_j is calculated with the help of the derivative matrix $\mathbf{D}$. The entries of $\mathbf{D}$ are computed from the derivative of the basis functions l_j,

$$D_{i,j} = l_j'(\xi_i). \tag{11}$$

For a 2-D element, the derivative matrices $\mathbf{L}_{\mathbf{D}_\xi}$ and $\mathbf{L}_{\mathbf{D}_\eta}$ with respect to ξ and η-axes, respectively, are constructed with the help of the Kronecker multiplication,

$$\mathbf{L}_{\mathbf{D}_\xi} = \mathbf{I} \otimes \mathbf{D}, \tag{12}$$

$$\mathbf{L}_{\mathbf{D}_\eta} = \mathbf{D} \otimes \mathbf{I}, \tag{13}$$

where $\mathbf{I}$ is the identity matrix.

The one-dimensional integral in (5) is approximated by Gaussian quadratures

$$\omega_j = \frac{2}{N(N+1)\left(L_N(\xi_j)\right)^2}. \tag{14}$$

The Gauss quadratures calculated in (14) are stored in a vector matrix $\boldsymbol{\omega}$. The two-dimensional integrals in (5), are approximated by 2-D quadratures

$$\mathbf{Q}_{2D} = \boldsymbol{\omega}\boldsymbol{\omega}^T. \tag{15}$$

The two-dimensional quadrature matrix, $\mathbf{Q}_{\xi,\eta}$, is obtained by rearranging $\mathbf{Q}_{2D}$ columnwise, resulting in a (N+1)^2 diagonal matrix.

B. Mapping in a curved side quadrilateral

In the case of complex geometries, one nonsquared or curved element can be applied instead of discretization into multiple elements. An example of such a quadrilateral is shown in Fig. 1c. The transformation of the computational domain to the desired quadrilateral is obtained by applying the transfinite interpolation method. The mapping, $\boldsymbol{X}(\xi,\eta)$, from the computational domain to an arbitrary quadrilateral is given by

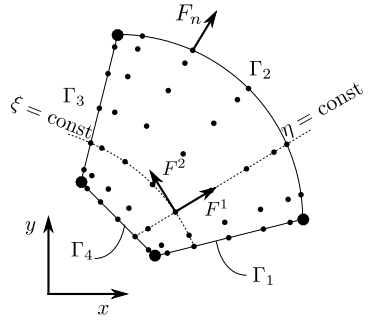

Fig. 2. A representation of the contravariant fluxes in an element with a curved boundary.

$$\begin{aligned}\boldsymbol{X}(\xi,\eta) = \frac{1}{2}\big((1-\xi)\boldsymbol{\Gamma}_4(\eta) + (1+\xi)\boldsymbol{\Gamma}_2(\eta) + (1-\eta)\boldsymbol{\Gamma}_1(\xi) \\ + (1+\eta)\boldsymbol{\Gamma}_3(\xi)\big) \\ - \frac{1}{4}\big((1-\xi)[(1-\eta)\boldsymbol{\Gamma}_1(-1) + (1+\eta)\boldsymbol{\Gamma}_3(-1)] \\ + (1+\xi)[(1-\eta)\boldsymbol{\Gamma}_1(1) + (1+\eta)\boldsymbol{\Gamma}_3(1)]\big),\end{aligned} \tag{16}$$

where $\boldsymbol{\Gamma}_k$ with index $k \in \{1, ..., 4\}$ represent the parametric description of the corresponding boundary. Rearranging the mapping gives

$$\boldsymbol{X}(\xi,\eta) = X(\xi,\eta)\hat{x} + Y(\xi,\eta)\hat{y}, \tag{17}$$

where $X(\xi,\eta)$ represents the mapping components related to the x-direction and $Y(\xi,\eta)$ the mapping components related to the y-direction

The transformation from the computational domain to the desired quadrilateral affects the derivative operators in (4). As a consequence, the chain rule should be applied to obtain the derivative under mapping. However, this requires the inverse of the transformation and is often unpractical to find. Alternatively, contravariant fluxes F^1 and F^2 which are normal to the ξ and η coordinate lines, respectively, are introduced and shown in Fig. 2. This allows operators such as the divergence and gradient to be written in terms of the mapping as shown in (5). Correspondingly, the contravariant fluxes F^1 and F^2 are given by

$$F^1 = c\frac{Y_\eta^2 + X_\eta^2}{J_T}\frac{\partial\varphi}{\partial\xi} - c\frac{Y_\xi Y_\eta + X_\xi X_\eta}{J_T}\frac{\partial\varphi}{\partial\eta}, \tag{18}$$

$$F^2 = -c\frac{Y_\xi Y_\eta + X_\xi X_\eta}{J_T}\frac{\partial\varphi}{\partial\xi} + c\frac{Y_\eta^2 + X_\eta^2}{J_T}\frac{\partial\varphi}{\partial\eta}. \tag{19}$$

The Jacobian determinant is computed as,

$$J_T = X_\xi Y_\eta - X_\eta Y_\xi. \tag{20}$$

The terms X_ξ, Y_ξ and Y_η, X_η are obtained from the chain rule, and represent the derivatives of the mapping functions with the respect to the ξ and η axes respectively.

The contravariant fluxes are evaluated for each LGL root of an element and the results are stored in a diagonal matrix with $(N+1)^2$ in size. By replacing the derivative operators

in (18) and (19) by its matrix equivalent as given in (12) and (13), the contravariant flux matrices $\mathbf{F}^1$ and $\mathbf{F}^2$ are obtained

$$\mathbf{F}^1 = \mathbf{C}[(\mathbf{Y}_\eta^2 + \mathbf{X}_\eta^2)\mathbf{L}_{\mathbf{D}_\xi} - (\mathbf{Y}_\eta\mathbf{Y}_\xi + \mathbf{X}_\eta\mathbf{X}_\xi)\mathbf{L}_{\mathbf{D}_\eta}]\mathbf{J}_T^{-1}\boldsymbol{\varphi}, \tag{21}$$

$$\mathbf{F}^2 = \mathbf{C}[(\mathbf{Y}_\xi^2 + \mathbf{X}_\xi^2)\mathbf{L}_{\mathbf{D}_\xi} - (\mathbf{Y}_\eta\mathbf{Y}_\xi + \mathbf{X}_\eta\mathbf{X}_\xi)\mathbf{L}_{\mathbf{D}_\eta}]\mathbf{J}_T^{-1}\boldsymbol{\varphi}, \tag{22}$$

where $\mathbf{C}$ is the matrix diagonal for the equation coefficient c. The normal flux, F_n, in (5), is orthogonal to the boundary of the domain as shown in Fig. 2. Depending on the orientation of the boundary, F_n will take the following expressions,

$$F_n = \begin{cases} \frac{|J_T|}{J_T}\sqrt{Y_\xi^2 + X_\xi^2}F^2, \text{ for } \boldsymbol{\Gamma}_1, \text{ and } \boldsymbol{\Gamma}_3, \\ \\ \frac{|J_T|}{J_T}\sqrt{Y_\eta^2 + X_\eta^2}F^1, \text{ for } \boldsymbol{\Gamma}_2, \text{ and } \boldsymbol{\Gamma}_4. \end{cases} \tag{23}$$

The flux, F_n, as presented in (5), is extensively used in applying different types of boundary conditions. Alternatively, the matrix form of the normal flux, $\mathbf{f}_n$, is given by

$$\mathbf{f}_n = \begin{cases} \text{sign}(\mathbf{J}_T)\sqrt{\mathbf{Y}_\xi^2 + \mathbf{X}_\xi^2}\mathbf{f}_b, \text{ for } \boldsymbol{\Gamma}_1, \text{ and } \boldsymbol{\Gamma}_3, \\ \\ \text{sign}(\mathbf{J}_T)\sqrt{\mathbf{Y}_\eta^2 + \mathbf{X}_\eta^2}\mathbf{f}_b, \text{ for } \boldsymbol{\Gamma}_2, \text{ and } \boldsymbol{\Gamma}_4, \end{cases} \tag{24}$$

where $\mathbf{f}_b$ is the flux forced on the boundary.

C. Matrix form of the nodal Galerkin method

The elliptic partial differential equation, as presented in (5), is described in its equivalent matrix form. The derivative operators are replaced by the derivative matrices from (12) and (13), the integrals are replaced by quadratures from (15). The matrix form of (5) for a single element with $\mathbf{f}_n$ zero on all boundaries is given by

$$-(\mathbf{L}_{\mathbf{D}_\xi^T}\mathbf{Q}_{\xi,\eta}\mathbf{F}^1 + \mathbf{L}_{\mathbf{D}_\eta^T}\mathbf{Q}_{\xi,\eta}\mathbf{F}^2)\boldsymbol{\varphi} = \mathbf{j}_T \circ \mathbf{s} \circ \boldsymbol{\omega}_{\xi,\eta}, \tag{25}$$

where $\boldsymbol{\varphi}$ is the column vector of the potential φ, $\mathbf{j}_T$ and $\mathbf{s}$ are the column vectors for the Jacobian determinant from (20) and the source term of the elliptic equation, respectively. If the potential vector $\boldsymbol{\varphi}$ is represented by an unknowns vector $\mathbf{u}$, the other terms from the left hand side are stored in a global matrix $\mathbf{E}$ and the source vector from the right hand side is represented by $\mathbf{b}$, the final linear system of equations given by

$$\mathbf{E}\mathbf{u} = \mathbf{b}. \tag{26}$$

D. Boundary conditions in matrix form

In order to solve the unknown field quantities at the LGL roots, various boundary conditions have to be considered. Four types of boundary conditions can be distinguished;

- Continuous boundary conditions;
- Dirichlet boundary conditions;
- Neumann boundary conditions;
- Robin boundary conditions.

Each of the previous mentioned boundary conditions are considered in the following subsections.

1) Continuous boundary condition

Continuity of the potential is preserved by the Galerkin formulation, the continuity of its first normal derivative is ensured by equaling the circular integral from (5) on the shared boundary. In the magnetic domain, the tangential component of the magnetic field strength is continuous at the boundary of neighboring elements. For the thermal domain, the temperature at the boundary between subsequent elements should be continuous. The continuity between the elements is preserved in the global matrix, $\mathbf{E}$, by the summation of the entries that have shared roots. Therefore, a shared boundary between elements is represented by a single row in the global matrix $\mathbf{E}$.

2) Dirichlet boundary condition

In order to force the z-component of the magnetic vector potential or, in case of the thermal domain, the temperature to a specific value, the Dirichlet boundary condition has to be applied. The Dirichlet boundary condition imposes a solution along the boundary giving

$$\varphi = u(x, y), \text{ on } \boldsymbol{\Gamma}_k, \tag{27}$$

where $u(x, y)$ represent the desired solution on the boundary and index k represents the index of the line. To implement the Dirichlet boundary condition, the entries of $\mathbf{b}$ in (26), that correspond to the lines and points where the condition is assigned, is given by

$$b_i = \varphi_i, \tag{28}$$

where φ_i is the imposed potential at the boundary and index i corresponds to the LGL roots on the boundary. The corresponding entries in global matrix $\mathbf{E}$ are replaced by a diagonal filled with ones.

3) Neumann boundary condition

Neumann boundary conditions appear at the interfaces of soft-magnetic materials. In this case, the first derivative of the magnetic vector potential has to satisfy

$$\frac{\partial\varphi}{\partial n} = u(x, y), \text{ on } \boldsymbol{\Gamma}_k, \tag{29}$$

For the implementation of this boundary condition, the circular integral from (5) is used. The normal flux in (23) is forced as a boundary condition. For soft-magnetic materials with infinite relative permeability, the tangential magnetic field strength at the interface must be zero giving

$$b_i = 0. \tag{30}$$

Unlike the case of Dirichlet boundary conditions, the corresponding rows in $\mathbf{E}$ remain unchanged. Similarly, (30) is applied in the thermal domain for perfectly insulating boundaries.

Furthermore, permanent magnets with homogeneous magnetization are taken into account by a Neumann boundary condition on the boundaries of the magnet region parallel to the magnetization direction. At these interfaces, the magnetization, M_0, of the permanent magnet is considered

$$b_i = f_{n\,i}M_0\omega_0 + j_{T\,i}s_i\omega_{\xi,\eta\,i}. \tag{31}$$

4) Robin boundary condition

The Robin boundary condition is a combination of the Dirichlet and Neumann boundary condition and occurs in the thermal domain at interfaces where convection is present. For the thermal domain, the Robin boundary condition is given by

$$k\frac{\partial T}{\partial n} + hT = hT_\infty, \text{ on } \mathbf{\Gamma}_k, \tag{32}$$

where h is the convection coefficient and T_∞ is the ambient temperature. In a similar way, the linearized thermal radiation can be included with a radiation heat transfer coefficient.

To implement this boundary condition, the operator $\mathbf{f}_n$ on the boundary flux is used obtaining on the right hand side,

$$b_i = -f_{n\,i} h T_\infty \omega_0 + j_{T\,i} s_i \omega_{\xi,\eta\,i}. \tag{33}$$

Furthermore, the global matrix $\mathbf{E}$ is summed with a diagonal matrix $\mathbf{T}$ which has the diagonal entries as

$$T_{ii} = -f_{n\,i} h. \tag{34}$$

IV. Nonlinearity and Losses of Soft-Magnetic Materials

A. Nonlinearity of soft-magnetic parts

Given that the coefficient c can be represented as a function of φ, the nonlinear material properties can be also modeled. The nonlinearity of the relative permeability of the soft-magnetic parts in the geometry is taken into account by iterating the field solution until convergence is obtained. The Newton-Raphson method is employed, with a relaxation coefficient of 0.8, to update the reluctivity of the soft-magnetic parts. The solution is obtained if the maximum discrepancy of the reluctivity between two consecutive iterations is lower than 10. The initial value for the reluctivity is at least 1000, therefore, convergence is obtained if the discrepancy is less than 1%. Similarly, the nonlinearity of the electrical conductivity with respect to the temperature is taken into account. In this case, convergence is obtained if the maximum temperature change between successive iterations is less than 0.1^oC.

B. Iron loss computation

The iron loss calculation in the soft-magnetic parts is based on the loss separation model of Bertotti [19]. The iron losses, q_{fe}, are computed on the roots of the Legendre-Gauss-Lobatto polynomial with degree N, resulting in (N+1)^2 entries for each element with soft-magnetic material properties. The computation of the hysteresis losses, P_{hys}, eddy current losses, P_c, and the excess losses, P_{ex}, over time τ are given by

$$q_{fe} = \frac{1}{\tau}\int_0^\tau P_{hys} + P_c + P_{ex}\mathrm{d}t \tag{35}$$

where,

$$P_{hys} = c_h B^2 f, \tag{36}$$

$$P_c = \sigma\frac{d^2}{12}\left(\frac{dB(t)}{dt}\right)^2, \tag{37}$$

TABLE I
Dimensions and Material Parameters of the Linear Actuator.

Symbol	Value	Description
h_1	4 mm	Height from the origin of the magnet array
h_2	5 mm	Height from the origin of the airgap
h_3	15 mm	Height from the origin of the phase slots
h_4	20 mm	Height from the origin of the translator
D	100 mm	Depth of the domain
τ_m	12 mm	Pole pitch of the permanent magnets
α_m	2/3	Permanent magnet width ratio
τ_c	16 mm	Pole pitch of the phase coils
t_{ins}	1 mm	Thickness of the insulation
α_m	9/16	Phase-slot width ratio
B_{rem}	1.2 T	Remanent flux density of permanent magnets
$\mu_{r,pm}$	1	Relative permeability of permanent magnets
k_{iron}	28 W/m·K	Thermal conductivity of iron
k_{coil}	1 W/m·K	Thermal conductivity of coil
k_{ins}	0.5 W/m·K	Thermal conductivity of the insulation
h_{conv}	10 W/m^2·K	Convection coefficient of non-forced air cooling
T_{amb}	20 ^{o}C	Ambient temperature
v_x	1 m/s	Velocity of the translator
J_p	1.56 A/mm^2	Peak current density

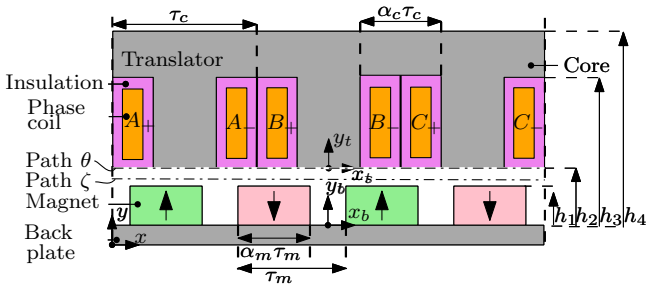

Fig. 3. A periodic section of the linear synchronous motor.

and

$$P_{ex} = c_e\left(\frac{dB(t)}{dt}\right)^{1.5}, \tag{38}$$

where

$$f = \frac{v_x}{2\tau_m}, \tag{39}$$

c_h is the hysteresis loss coefficient, c_e the excess losses coefficient, v_x the velocity of the mover, τ_m the pole pitch of the permanent magnet array and B is the spatial distribution of the magnetic flux density. The hysteresis and excess losses coefficients are determined by fitting the loss model with the soft-magnetic material losses provided by the manufacturer.

V. Comparison with Finite Element Method

The validation of the spectral element model for the magnetic and thermal domain is performed on a periodic section of a linear synchronous machine, as shown in Fig. 3.

A. Model assumptions and boundary conditions

The investigated geometry comprises of three phases with concentrated windings and 4 surface mounted permanent magnets, attached to a solid iron back plate. The magnetization direction of the permanent magnets, with remanent flux density B_{rem}, is indicated by the direction of the arrows whereas the

phase coils are indicated by uppercase A, B and C. An insulating compound, with thickness t_{ins}, is present in the slotted structure, surrounding the phase coils. The laminated iron core of the translator consists of M400-50A [20]. Dimensions and material properties of the investigated geometry are given in Table I.

To obtain a field solution based on the spectral element method as derived in Section III, the problem should be described by a 2-D model. Most electromagnetic devices have a 3-D geometry, therefore, the geometry should be invariant with one of the three dimensions, or its dependency should be negligible. This assumption is generally valid since, for example, the 3-D effects due to the finite axial length in rotary actuators are often negligible. The motor geometry as presented in Fig. 3 is assumed to be periodical with respect to the y-direction. Therefore, the periodic boundary condition is applied along $y-$axis at $x = 4\tau_m$. For the magnetostatic case, the z-component of the vector potential, A_z, is assumed to be zero at the top of translator (y = 25 mm). The Neumann boundary condition is applied on the bottom side of the back plate, mimicking soft-magnetic material with infinite permeability. For the steady-state thermal modeling, a convection boundary is applied to the top (y = 25 mm) and bottom (y = 10 mm) boundary of the translator. For natural convection, the convection coefficient, h_{conv} is in the range of 10 - 30 [21]. For this scenario, a relative conservative value of 10 W/m^2·K is adopted as the convection coefficient.

For the purpose of verification, relevant field quantities are extracted on path θ and ζ. Both paths are lines parallel to the x-axis. Path θ is located at the bottom of the translator and is used to validate the temperature distribution. Path ζ is centered in the airgap and is used to assess the convergence and accuracy of the magnetic field distribution. If the geometry of Fig. 3 is considered for its initial position (Δ_x=0mm) the current densities for the A, B and C phase are respectively given by

$$J_A = J_p \cos\left(\frac{\Delta_x \pi}{\tau_p} + \frac{2}{3}\pi\right), \quad (40)$$

$$J_B = J_p \cos\left(\frac{\Delta_x \pi}{\tau_p}\right), \quad (41)$$

$$J_C = J_p \cos\left(\frac{\Delta_x \pi}{\tau_p} - \frac{2}{3}\pi\right), \quad (42)$$

where J_p is the peak current density.

B. Convergence analysis

In the absence of an analytical solution for the linear motor geometry, the results obtained with SEM are compared with the finite element analysis model with a fine mesh, such that the self-convergence (i.e. the maximum error between successive mesh iterations) is below 1%, is chosen as a reference. A total of 48043 second-order triangular mesh elements are required to obtain the desired accuracy. The convergence of the discrepancy of the x and y-components of the magnetic flux density along path ζ for both SEM and FEM is shown in Fig. 4. Mesh distributions of the finite element model, belonging to the results of point A and B

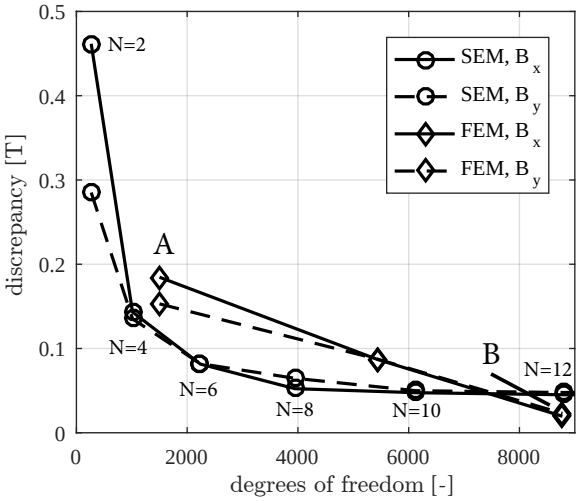

Fig. 4. The convergence of the SEM solution along path ζ as function of the degree of the LGL polynomial.

of Fig. 4, are shown in Fig. 5. For the polynomial degree N = 4 to N = 10, the spectral element model obtains higher accuracy for fewer degrees of freedom. For N equal to 6, the spectral element method requires approximately a third of the number of unknowns (2239 degrees of freedom) compared to the finite element analysis (5501 degrees of freedom) for the same accuracy. The magnetic flux density in the airgap, as shown in Fig. 6, shows good agreement with the results of finite element reference model. The maximum discrepancy between the spectral element method and the finite element analysis is 0.08 T and, hence, a relative discrepancy less than 6.5 %.

The force production in the x and y-directions are obtained at the initial position of the translator (Δ_x=0mm) by applying the Maxwell stress tensor. According to the spectral element method with N equal to 6, the forces are 19.4 and -254.5 N in the x and y-direction, respectively. Compared to the finite element analysis, which obtained 18.9 and -247.3 N respectively, a discrepancy less than 3 % is observed. Further comparison of the spectral element model is performed for N = 6 since the results are in good agreement with finite element analysis for this degree. In Fig. 7, the LGL nodal distribution for N =

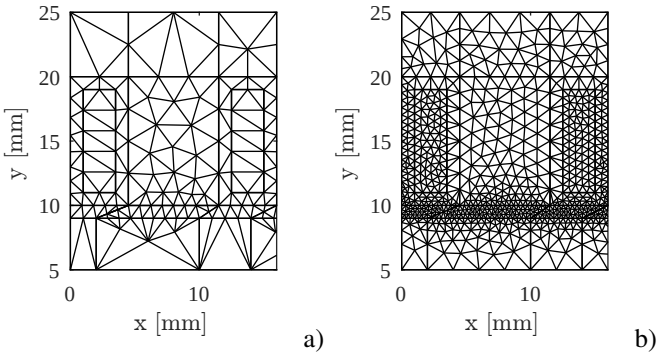

Fig. 5. a) The coarse mesh with 1500 degrees of freedom of the finite element analysis of mesh distribution A in Fig. 4. b) The fine mesh with 8766 degrees of freedom of the finite element analysis of mesh distribution B in Fig. 4

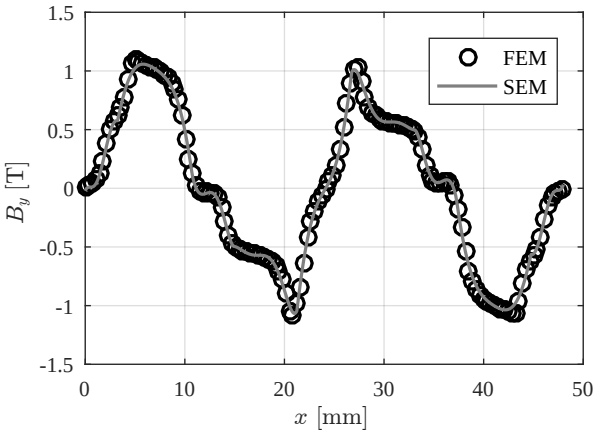

Fig. 6. The y-component of the magnetic flux density along path ζ for both SEM and FEM.

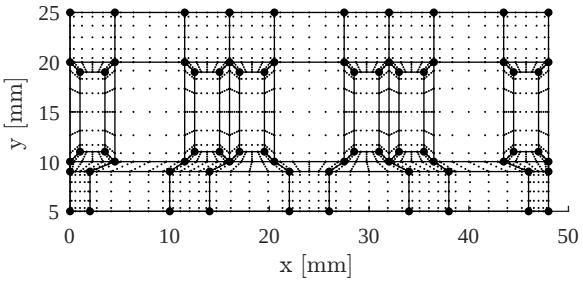

Fig. 7. The distribution of roots for $N = 6$ in the linear synchronous motor geometry.

6 of the investigated linear motor geometry is illustrated.

The convergence analysis from the Fig. 4 shows, in fact, the advantages of SEM. The accuracy of SEM is improved by using elements with a high degree polynomial equal to N. Consequently, in the case of the magnetic flux density, the curl of the magnetic vector potential A_z is computed based on the $N \times N$ nodes from the given element. The error is decreasing when N is increased [10]. In the case of second order elements in FEM, the derivative is computed based on three neighboring nodes only, making the method less accurate with the respect to SEM.

C. Validation of the magnetic field

The magnetic flux density distribution in the translator, obtained by SEM, is shown in Fig. 8a for x_s coinciding with x_t. The discrepancy with finite element analysis is shown in Fig. 8b. The average relative error is 2 % for the entire geometry. A clear discrepancy of 0.5 [T] is found in the corners with soft-magnetic material where relative high magnetic flux densities are present. The large discrepancy in the corners of the soft-magnetic parts is related to the singularities which appear due to the abruptly changing line describing the corner geometry, at the corner point it remains continuous, but the derivatives are discontinuous. These singularities can be avoided by applying a rounding radius to the corner [10]. In [22], different rounding radii of the corner are investigated for a transformer with a core without airgap. It has been shown that even for a small radius, the discrepancy with FEM results

TABLE II
COEFFICIENTS OF M400-50A FOR BERTOTTI IRON LOSS CALCULATION.

σ_{iron}	$2 \cdot 10^6$ S/m	Electrical conductivity
ρ_{iron}	7850 kg/m^3	Mass density
c_{h100}	210.5 Wsm^3/T^2	Hysteresis loss coefficient for 100 Hz
c_{e100}	0.3778 Wm^3/(T/s)$^{1.5}$	Excess loss coefficient for 100 Hz
c_{h200}	272.5 Wsm^3/T^2	Hysteresis loss coefficient for 200 Hz
c_{e200}	0.1806 Wm^3/(T/s)$^{1.5}$	Excess loss coefficient for 200 Hz
c_{h400}	372.7 Wsm^3/T^2	Hysteresis loss coefficient for 400 Hz
c_{e400}	0.05 Wm^3/(T/s)$^{1.5}$	Excess loss coefficient for 400 Hz
t_l	0.5 mm	Lamination thickness
c_f	1	Stacking factor

becomes smaller. This behavior will remain valid for other geometries as well.

D. Validation of the loss separation

The distribution of the iron losses in the translator are obtained for a total displacement of two pole pitches, τ_m, with different constant velocities of the mover, v_x, of 2.4, 4.8 and 9.6 m/s. These velocities correspond with a excitation frequency of 100, 200 and 400 Hz, respectively. The hysteresis and excess loss coefficients are obtained by fitting the loss data supplied by the manufacturer [20] and are given in Table II. The iron losses computed by the spectral element method are obtained for $N = 6$ whereas the iron losses from the finite element method are obtained using the mesh shown in Fig. 5b. The separate loss components for both the spectral element and the finite element method are shown in Fig. 9. A good agreement is obtained for the separate loss contributions over the investigated frequency range. On average, the discrepancy between the loss computation of the spectral element method and the finite element method is 5.4 %. This discrepancy is caused by inaccuracies in the magnetic field computation near corner singularities. In the area near these corners, high magnetic field intensities are present, and therefore, have a significant contribution to the prediction of the losses since the hysteresis and eddy current losses increase quadratically with the magnetic flux density.

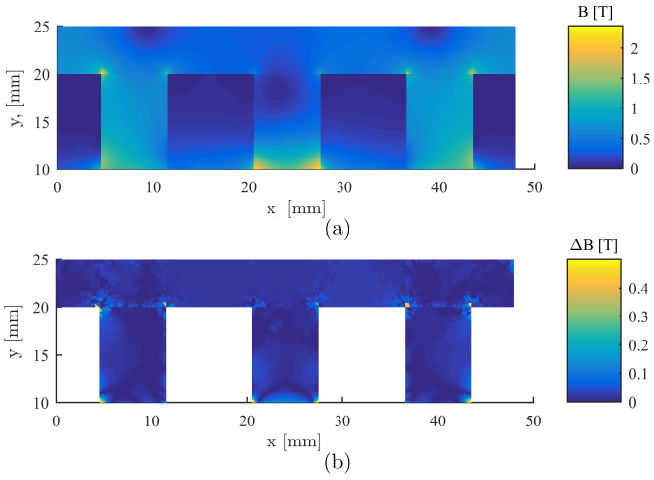

Fig. 8. a) The magnetic flux density in the translator. b) The absolute error, ΔB, of the magnetic flux density in the translator with respect to FEM.

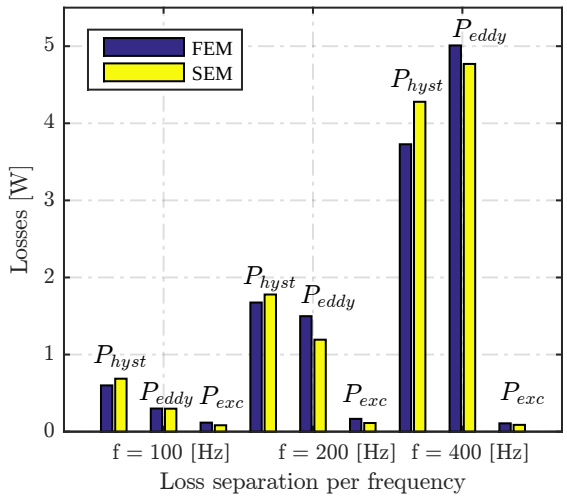

Fig. 9. Comparison of the iron losses in the soft-magnetic parts of the translator between SEM and FEM

E. Validation of temperature distribution

The thermal losses in the investigated motor geometry can be classified into ohmic losses, i.e. conduction losses in the phase coils, and iron losses. These losses are implemented as volumetric heat sources. The temperature field is obtained with respect to the ambient temperature, T_∞, of 20 ^{o}C. The thermal conductivity of the phase coils is considered to be equal to 1 W/m·K, representing the conductivity of the copper and the wire insulation. The temperature distribution of the translator for the losses at 200 Hz is shown in Fig. 11. The temperature along path θ obtained by the spectral element and the finite element method is shown in Fig. 10. From this figure it is clear that a discrepancy of 0.4 ^{o}C is present between SEM and FEM for an average temperature increase of 37.5∘C. This discrepancy is related to the implementation of losses in the used finite element package. In SEM, the iron losses are computed spatially and also treated as a spatially distributed heat source. In the finite element package, losses are distributed isotropically within a region and, therefore, neglecting any spatial content. Subsequently, the distribution

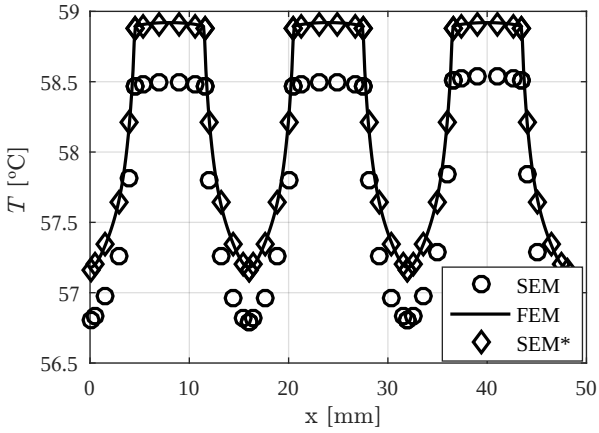

Fig. 10. Comparison of the temperature computed by SEM and FEM on path θ. SEM* indicates the temperature distribution computed with SEM and using the losses distribution as in the finite element analysis.

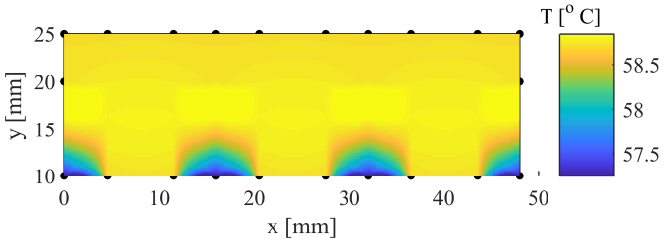

Fig. 11. (a) The temperature distribution in the translator (SEM) with respect to an ambient temperature, T_{amb}, of 20 ^{o}C.

of the iron losses in SEM in the same manner as the finite element package results in lower discrepancy, as shown by the diamond markers in Fig. 10. In this case, the discrepancy is lower than 0.07 ∘C.

VI. Conclusion

In this paper, the general formulation of spectral element analysis for solving static magnetic field and temperature distributions in 2-D boundary value problems is presented. The different types of boundary conditions are discussed as well as their implementation and application for both domains for a periodic section of the linear synchronous motor. The convergence analysis indicated that a higher accuracy is obtained for low-degree spectral polynomials compared to finite element analysis with equal number of unknowns. Depending on the desired accuracy, up to three times less degrees of freedom are required in the spectral element method compared to the finite element method. The accuracy of the spectral element model is limited by singularities in the corner of the soft-magnetic parts. This can be avoided by modeling the iron geometry with rounded corners. A good agreement is obtained with respect to finite element analysis in terms of the magnetic flux density and temperature distribution as well as the iron loss computation for different frequencies and the force production. This shows the applicability of the spectral element model to perform coupled magnetic-thermal analysis of electromagnetic devices with fewer degrees of freedom and, hence, lower computational load compared to finite element analysis.

Appendix A
Derivation of the Galerkin formulation

In the subsection II-B the equation (4) stands for the Galerkin formulation in a computational element, which is a square with the limits $[-1, 1]^2$ when using LGL nodes. However, in the case of nonsquared or curved boundaries elements, the mapping functions are used such as those described in the subsection III-B. Therefore, the gradient and divergence operators from (1) are evaluated under mapping such that:

$$\nabla\varphi = \frac{1}{J_T}\left[\left(Y_\eta\frac{\partial\varphi}{\partial\xi} - Y_\xi\frac{\partial\varphi}{\partial\eta}\right)\hat{x} + \left(-X_\eta\frac{\partial\varphi}{\partial\xi} + X_\xi\frac{\partial\varphi}{\partial\eta}\right)\hat{y}\right] \tag{43}$$

The derivatives along the x and $y-$axis, respectively could be considered as the covariant fluxes F_1 and F_2, the expression for the gradient is obtained as

$$\nabla\varphi = \frac{1}{J_T}\left(F_1\hat{x} + F_2\hat{y}\right). \tag{44}$$

The expression for the divergence it is obtained with the contravariant fluxes

$$\nabla\cdot\mathbf{F} = \frac{1}{J_T}\left(\frac{\partial}{\partial\xi}F^1 + \frac{\partial}{\partial\eta}F^2\right), \tag{45}$$

where the contravariant fluxes are expressed from covariant ones

$$F^1 = \quad Y_\eta F_1 - X_\eta F_2 \tag{46}$$

$$F^2 = \quad -Y_\xi F_1 + X_\xi F_2. \tag{47}$$

By writing the equation (1) in a physical domain, and applying the same procedure as in subsection II-B with (45), it is obtained

$$\iint\limits_{\Omega_{x,y}}\left[\frac{\partial}{\partial\xi}(F^1) + \frac{\partial}{\partial\eta}(F^2)\right]\beta\mathrm{d}\Omega_{x,y} = \iint\limits_{\Omega_{x,y}} s\mathcal{J}_T\beta\mathrm{d}\Omega_{x,y}, \tag{48}$$

by applying the integration by parts, the equation (5) is obtained.

ACKNOWLEDGMENT

This paper is part of the project ADvanced Electric Powertrain Technology (ADEPT) funded by EU - Marie Curie ITN, grant number 607361.

REFERENCES

[1] B. L. J. Gysen, K. J. Meessen, J. J. H. Paulides, and E. A. Lomonova, "General Formulation of the Electromagnetic Field Distribution in Machines and Devices Using Fourier Analysis," *Magnetics, IEEE Transactions on*, vol. 46, no. 1, pp. 39–52, 1 2010.

[2] E. Ilhan, J. Paulides, L. Encica, and E. Lomonova, "Tooth contour method implementation for the flux-switching PM machines," in *The XIX International Conference on Electrical Machines - ICEM 2010*. IEEE, 9 2010, pp. 1–6.

[3] Z. Zhu, D. Howe, and C. Chan, "Improved analytical model for predicting the magnetic field distribution in brushless permanent-magnet machines," *IEEE Transactions on Magnetics*, vol. 38, no. 1, pp. 229–238, 2002.

[4] M. Markovic, M. Jufer, and Y. Perriard, "Reducing the Cogging Torque in Brushless DC Motors by Using Conformal Mappings," *IEEE Transactions on Magnetics*, vol. 40, no. 2, pp. 451–455, 3 2004.

[5] T. A. Driscoll and L. N. Trefethen, *Schwarz-Christoffel mapping*. Cambridge University Press, 2002.

[6] K. J. W. Pluk, J. W. Jansen, and E. A. Lomonova, "3-D Hybrid Analytical Modeling: 3-D Fourier Modeling Combined With Mesh-Based 3-D Magnetic Equivalent Circuits," *IEEE Transactions on Magnetics*, vol. 51, no. 12, pp. 1–14, 12 2015.

[7] K. Ramakrishnan, M. Curti, D. Zarko, G. Mastinu, J. J. H. Paulides, and E. A. Lomonova, "Comparative Analysis of Various Methods for Modelling Permanent Magnet Machines," *IET Electric Power Applications*, 1 2017.

[8] J. W. Jansen, J. P. C. Smeets, T. T. Overboom, J. M. M. Rovers, and E. A. Lomonova, "Overview of Analytical Models for the Design of Linear and Planar Motors," *IEEE Transactions on Magnetics*, vol. 50, no. 11, pp. 1–7, 11 2014.

[9] Yang Tang, J. J. H. Paulides, and E. A. Lomonova, "Automated Design of DC-Excited Flux-Switching In-Wheel Motor Using Magnetic Equivalent Circuits," *IEEE Transactions on Magnetics*, vol. 51, no. 4, pp. 1–11, 4 2015.

[10] J. P. Boyd, *Chebyshev and Fourier spectral methods*. Springer-Verlag, 1989.

[11] D. A. Kopriva and J. H. Kolias, "A Conservative Staggered-Grid Chebyshev Multidomain Method for Compressible Flows," *Journal of Computational Physics*, vol. 125, no. 1, pp. 244–261, 4 1996.

[12] I. Mahariq, M. Kuzuoglu, I. H. Tarman, and H. Kurt, "Photonic Nanojet Analysis by Spectral Element Method," *IEEE Photonics Journal*, vol. 6, no. 5, pp. 1–14, 10 2014.

[13] Y. Peet and P. Fischer, "Legendre spectral element method with nearly incompressible materials," *European Journal of Mechanics - A/Solids*, vol. 44, pp. 91 – 103, 2014.

[14] H. P. Pfeiffer, L. E. Kidder, M. A. Scheel, and S. A. Teukolsky, "A multidomain spectral method for solving elliptic equations," 2 2002.

[15] *Altair FLUX2D User's Guide*, Altair Engineering Inc., 2017.

[16] M. N. Ozsk, *Heat conduction*. Wiley, 1993.

[17] C. W. Mastin, *Fundamentals of Grid Generation (P. Knupp and S. Steinberg)*. Society for Industrial and Applied Mathematics, 6 1995, vol. 37, no. 2.

[18] D. A. Kopriva, *Implementing Spectral Methods for Partial Differential Equations*, ser. Scientific Computation. Springer, 2009.

[19] F. Fiorillo and A. Novikov, "An improved approach to power losses in magnetic laminations under nonsinusoidal induction waveform," *IEEE Transactions on Magnetics*, vol. 26, no. 5, pp. 2904–2910, Sep 1990.

[20] "Datasheet SURA M400-50A."

[21] J. Lienhard and J. Lienhard, *A Heat Transfer Textbook*. PhLogiston press, 2017.

[22] M. Curti, J. W. Jansen, and Lomonova E. A., "Convergence Analysis of Spectral Element Method for Electromechanical Devices," in *18th International Symposium on Electromagnetic Fields in Mechatronics, Electrical and Electronic Engineering*, Lodz, 2017.